1	Hydrospheric modulation of stress and seismicity on shallow faults in southern
2	Alaska
3	
4	Christopher W. Johnson 1, Yuning Fu 2, and Roland Bürgmann 3
5 6	¹ Scripps Institution of Oceanography, University of California San Diego, La Jolla, California, 92093, USA
7 8	² School of Earth, Environment and Society, Bowling Green State University, Bowling Green, Ohio 43403, USA
9 10	³ Berkeley Seismological Laboratory, University of California Berkeley, Berkeley, California 94720, USA
11	
12	Corresponding author: Christopher W. Johnson (cwj004@ucsd.edu)
13	
14	Highlights:
15	 Hydrospheric induced stress time series derived from GRACE solutions from 2002-2016
16	• Seasonal stress changes are used to assess the influence of surface loading on faults
17 18	• Seismicity rates are greatest 3 months after the reduction in mean normal stress

Abstract

Shallow (≤40 km), low magnitude (M≥2.0) seismicity in southern Alaska is examined for seasonal variations during the annual hydrological cycle. The seismicity is declustered with a spatio-temporal epidemic type aftershock sequence model. The removal of aftershock sequences allows detailed investigation of seismicity rate changes as water, snow and ice loads modulate crustal stresses throughout the year. The GRACE surface loads are obtained from the JPL global land and ocean mass concentration blocks (mascon) solutions. The stress changes at a depth of 10 km are calculated using a 1D spherical layered Earth model. To evaluate the induced seasonal stresses of ~10 kPa, we use >30 years of earthquake focal mechanisms to constrain the tectonic background stress field orientation and assess the seasonal stress change with respect to the principal stress orientations. The background stress field is assumed to control the preferred orientation of faulting, and stress perturbations are expected to increase or decrease seismic activity on the faults. The number of excess earthquakes is calculated with respect to the background seismicity rates for discrete stress intervals. The results indicate a ~25% increase in regional seismicity rates that correlate with a ~3-month time lag following failure-encouraging annual mean-normal-stress, differential stress, and least principal compressive stress. No immediate earthquake rate variations are observed in this region-wide analysis. The correlation with a 3-month time lag suggests increased mobility of preexisting fluids at seismogenic depths is varying the pore pressure within fault zones to modulate the seismicity rates throughout the seasonal loading cycle.

1 Introduction

In southern and central Alaska, seasonal changes in hydrological loading are observed geodetically with both the Global Positioning System (GPS) and the Gravity Recovery and Climate Experiment (GRACE). During the fall and winter months, the precipitation and snow accumulation produces crustal subsidence on the order of 1-3 cm [Fu et al., 2012]. On time-scales longer than an annual cycle, southern Alaska is experiencing a net loss of glacial ice that has accelerated in recent years [Larsen et al., 2015]. The rapid loss of ice mass during the 20th century is estimated to have produced stress changes between 200 - 1200 kPa, and is thought to be associated with a long-term background seismicity rate increase in southern Alaska [Sauber and Molnia, 2004; Sauber and Ruppert, 2008].

The seismic response to an applied stress transient on an active fault system is complicated and is not yet fully understood. Tectonic forces are generally considered a source of steady loading and result in mainshocks that are distributed randomly in space and time [e.g. *Gardner and Knopoff*, 1974]. These mainshocks produce localized stress increases triggering near-field aftershock sequences that decay exponentially with time and can produce stress shadows in which seismicity rates are reduced [e.g. *Felzer et al.*, 2002; *Toda et al.*, 2012]. Postseismic relaxation processes further modify tectonic stress and seismicity rates [e.g. *Freed*, 2005]. If subtle changes in static stress influence the timing of earthquakes, either promoting or discouraging nucleation, then one could expect that earthquakes will occur more often during periods of preferential surface loading conditions. Surface loading can produce stress changes on the order of 10⁰-10³ kPa and variations in seismicity correlated with hydrospheric, atmospheric, thermal, and tidal loads provide evidence for a causal relationship between surface processes and the modulated release of tectonic strain [*Heki*, 2003; *Hainzl et al.*, 2006; *Christiansen et al.*,

62 2007; Bettinelli et al., 2008; Hainzl et al., 2013; Amos et al., 2014; Craig et al., 2017; Johnson et al., 2017a; b].

The complex network of crustal faulting above a subduction zone makes Alaska an ideal natural laboratory to explore the modulation of seismicity during surface mass changes. The active tectonics of southern Alaska include the subduction zone and shallow, inland crustal faults, both of which are capable of hosting large magnitude earthquakes. In the Alaska subduction zone, the Pacific plate and the Yakutat block are thrusting beneath the North American plate and the plate interface hosted the 1964 $M_w9.2$ Great Alaskan earthquake, which is the second largest instrumentally recorded event. Inland from the subduction zone is the location of the 2002 $M_w7.9$ Denali Fault earthquake, which initiated on a thrust fault before stepping onto the Denali and Totschunda strike-slip faults and rupturing for ~340 km [Eberhart-Phillips et al., 2003].

2 Data and methods

64

65

66 67

68

69

70

71

72 73

74

75

76 77

78 79

80

81

82

83

84

85

86

87

88

89

90

91

92

93

94 95

96

97 98

99

100

101

102

103

104105

2.1 Data

2.1.1 Earthquake hypocentral locations and focal mechanisms

The hypocentral and focal mechanism catalogs are produced by the Alaska Earthquake Center (earthquake.alaska.edu) and contain seismicity records and focal plane solutions for historic events dating back to 1927. The seismic network is most densely concentrated in southern Alaska to monitor activity on crustal faults, the subduction zone, and along the Aleutian Islands. Non-tectonic events, notably glacial activity [O'Neel et al., 2007; O'Neel et al., 2010], are tagged and removed to retain only earthquakes for the analysis. The study area is limited to 156°W - 135°W and 59°N – 66°N to focus only on southern Alaska. The events before 2000 and below M0.0 are not considered in the analysis to maintain temporal consistency with the surface loading data, but are evaluated to demonstrate variations in the longer history of annual seismic activity. We retain shallow events above 40 km depth for latitudes north of 62° and in a separate study will consider the plate interface and intra-slab events. South of 62° and below the Talkeetna Mountains the depth range is limited to 20 km to reduce mixing crustal earthquakes with those located in the shallow subducting slab below Kenai Peninsula and Prince William Sound [Ruppert, 2008]. The resulting hypocentral catalog contains 174,147 events with a median depth of 8.8 km. The magnitude of completeness (M_c) is estimated using the entire-magnituderange method [Woessner and Wiemer, 2005] where the best-fit model assumes a cumulative normal distribution for the number of events less than the M_c and a log-normal distribution for events above the M_c. The data is divided into 0.5° non-overlapping regions to estimate the spatially variable M_c across the study area. The catalog M_c is found to be between $M_c1.1 - M_c1.6$ for onshore regions across southern Alaska and increases to M_c 2.0 offshore (Figure 1). The spatial variability in the M_c values is related to regional station coverage and the ability to consistently detect and locate lower-magnitude events. The temporal variations in M_c show lower values during the early 1980's (Figure S1) when most detected events were at latitudes south of 63° (Figure S2), then increasing to M_c 2.0 during the late 1980's before stabilizing between M_c1.0 - M_c1.5 in the years following 2003. Some of these variations through time are attributed to changes in data processing practices between 1971-1999 to calculate the local and moment magnitudes [Ruppert and Hansen, 2010]. With the installation of the Transportable Array in Alaska [http://www.usarray.org/Alaska], the expectation is a lower M_c throughout much of the region in future studies.

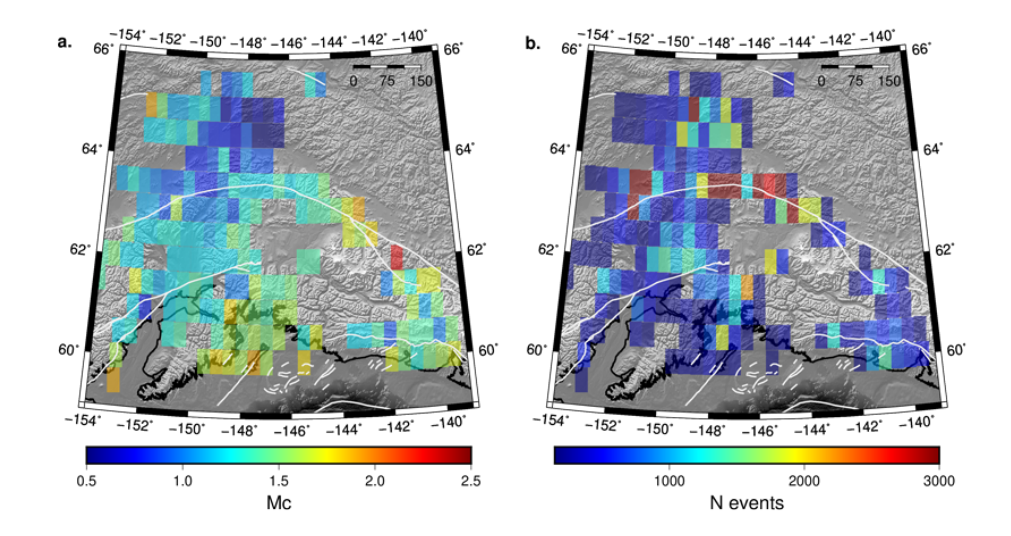


Figure 1. (a) The hypocentral catalog magnitude of completeness (M_c) is shown for southern Alaska on a 0.5° grid using all M \geq 0.0 seismicity data available from 2000-2017. The white lines are the major fault traces in the region. (b) The number of 2000-2017 catalog events used in each grid patch.

The focal mechanism catalog is selected following the same spatiotemporal criteria and contains 1,963 events, which is significantly less than the hypocentral catalog. Calculating a focal solution requires analysts manually picking first motions, a minimum number of observations for a stable solution, and good azimuthal coverage of the focal sphere [e.g. *Hardebeck and Shearer*, 2002]; hence the large discrepancy in the total number of events when compared to the more automated production of a hypocentral catalog. The focal mechanisms are used to estimate the background stress orientation, and throughout the analysis the two catalogs are treated independently due to the inherent differences.

2.1.2 GRACE derived terrestrial water storage

The changes in terrestrial water storage are obtained from the GRACE observations of gravity changes. The data product used is the Jet Propulsion Laboratory RL05M Mass Concentration Blocks (mascons) solution that is calculated for a near monthly gravity change for each 3° mascon (ftp://podaac-ftp.jpl.nasa.gov/allData/tellus/L3/mascon/RL05/JPL/CRI/netcdf/accessed 20 June 2017) in equivalent water thickness [*Watkins et al.*, 2015]. The data set includes 147 solutions from early 2002 through 2016. The monthly solution for each mascon represents the relative change from the baseline average from January 2004 to December 2009. The solutions are provided on a 0.5° grid, but the actual resolution of the mass change is reflected in the 3° mascon. To remove the sharp boundaries between neighboring mascons we apply a 450-km radius Gaussian filter to produce a more realistic, continuous representation of the surface loads for the stress-change modeling (Figure 2). The smoothed global solutions are limited to the region -160° to -120° in longitude and 50° to 70° in latitude. In this study, we are interested in the seasonality of the loading cycle and remove the interannual trend using a 36-month moving average and focus on the annual cycles.

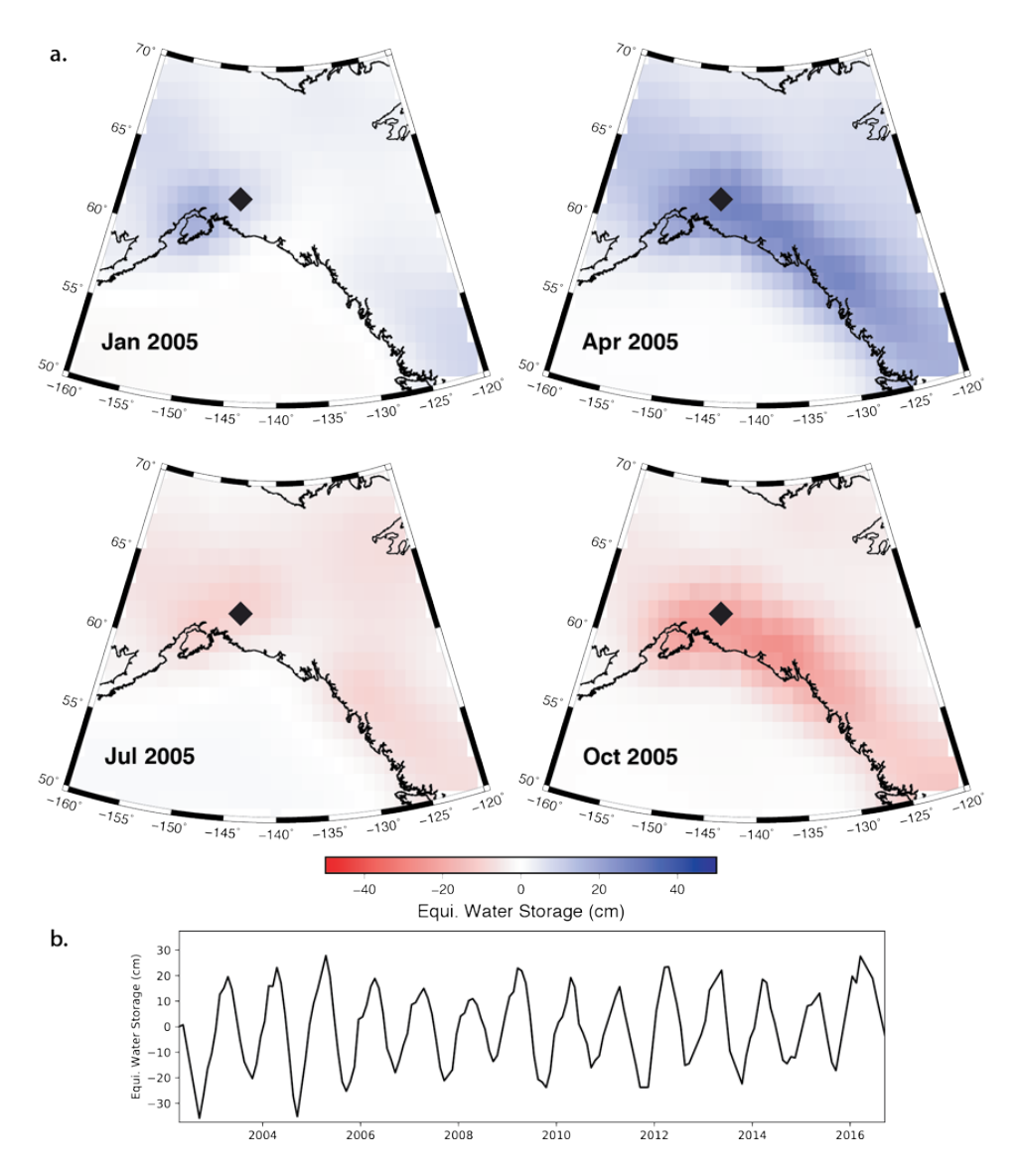


Figure 2. (a) GRACE derived seasonal terrestrial water storage shown for 2005. The original L3 mascon data is smoothed using a 450 km Gaussian filter to remove the sharp boundaries between blocks and detrended to focus on the seasonal variations. (b) The detrended time series shows the equivalent water storage for the location indicated by the black diamond.

2.2 Methodology

The seismicity and water storage data inform various models which are used to quantify seasonal surface loading and the statistical significance of associated changes in seismic activity. Modeling the seismicity data removes aftershocks and retains independent events to reduce any bias in the number of earthquakes occurring at any given time. Mechanical models are developed to estimate the seasonal stress changes due to the hydrospheric surface loading derived from the GRACE time series. To assess the degree of correlation between the seasonal stress changes and the timing of the seismicity, we analyze the seasonal stress-tensor variations with respect to the ambient stress orientations obtained from the focal mechanism catalog and calculate the relative change in seismic activity from the background earthquakes.

2.2.1 Earthquake catalog declustering

Developing models to describe variations in seismicity rate requires careful attention to the exclusion of non-tectonic sources and the clustering introduced by earthquake aftershock sequences. The seismicity data is prescreened by analysts for non-tectonic events (i.e., quarry blasts, glacial activity, etc.), and the aftershock sequences are characterized with a point process model. We use a spatial temporal epidemic type aftershock sequence (ETAS) model to quantify the likelihood of each event being dependent or independent and follow the probability-based declustering algorithm in *Zhuang et al.* [2002] using a uniform distribution of random numbers to retain and remove events from the catalog.

2.2.2 Surface loading and crustal stress models

Loading models for surface mass change on a spherical non-rotating elastic sphere are used to estimate the stress variations in the shallow crust. The model assumes a 1-D Earth structure using the Preliminary Reference Earth Model [Dziewonski and Anderson, 1981] to estimate the elastic deformation from a vertical surface force distributed on a layered spherical Earth [Pollitz et al., 2013; Johnson et al., 2017a; b]. The GRACE derived terrestrial water storage is converted to a vertical force using the density of water to determine the mass per 0.5° grid patch. The model calculates a 6-component strain tensor for each grid patch at the time of each GRACE acquisition at a depth of 10 km, resulting in a near monthly strain-tensor time series. The corresponding stress-tensor time series is calculated from the strain tensors using Hooke's law, assuming a Poisson ratio of 0.25 and a shear modulus of 30 GPa for the entire study area. This provides a linear mapping to stress that is homogeneous throughout the region. Implementing a varying elastic structure is beyond the scope of this analysis and constant values are assumed [Ali and Freed, 2010]. The smoothing procedure applied to the GRACE data eliminates any abrupt change between each mascon where we would expect a more gradually changing stress field. The modeling effort produces a spatiotemporal representation of the varying stress relative to the absolute stress field in the crust, which allows the assessment of a possible relationship with changes in seismic activity.

2.2.3 Background stress field

The background stress field is estimated from the regional focal mechanism data that are gridded into 0.25° non-overlapping patches. A normalized 6-component stress tensor is inverted for each grid patch using the SATSI damped least squares algorithm that minimizes the difference of the shear stress vector on the focal plane and the slip vector [*Hardebeck and Michael*, 2006]. We perform a suite of inversions to determine the tradeoff between the model misfit and variance for a range of spatial damping parameters. Due to the limited number of events for the large study area all 2,013 focal mechanisms from 1970-2017 are included in the gridding procedure. Each grid patch must contain a minimum of 10 events to be included. To increase the number of valid locations, we also consider reducing the number of required events to 6 and then 3, which is highly unconstrained, for a patch and invert the data set for a new stress field. The procedure allows us to include additional data when estimating the stress field and assess changes in the tensor orientations as additional patches are included that contain less observations. The goal is to describe the background stress field with the largest coverage of the study area while maintaining a reliable inversion solution with the available data.

2.2.4 Seismicity modulation

The ambient stress orientation is used in conjunction with the seasonally varying stress tensor time series to assess changes aligned with the tectonic principal stress components [Johnson et al., 2017b]. The main assumption is that active faults in each grid patch are favorably aligned to that same orientation. Therefore, assessing the seasonal stress change in the orientation of the principal background components will indicate if the surface loading is expected to promote or suppress earthquake activity on local faults. For the time of each earthquake, a 6-component seasonal loading stress-tensor is resolved at the event location. The seasonal stress tensor is projected into the orientation of the ambient stress field to extract the stress components that are unique to each earthquake in a grid patch at a given time. To assess a possible phase shift, the stress tensor 1 to 5 months prior to the event is associated with each earthquake. Additionally, the stressing rate is calculated from the stress-tensor time-series and evaluated for each event. Here we focus on changes in the maximum and minimum principal stresses σ_1 and σ_3 , the differential stress ($\sigma_1 - \sigma_3$), and the mean-normal-stress ($\sigma_1 + \sigma_2 + \sigma_3$)/3, where our sign convention is positive for tension and negative for compression. We evaluate the modulation of seismicity using Equation 1 by quantifying the percentage of expected earthquakes occurring within a discrete stress interval assuming constant background seismicity rates with respect to the events actually observed during the seasonally varying load.

$$N_{Ex} = \frac{(Act - Exp)}{Exp} \times 100 (1)$$

182183

184 185

186

187

188 189

190

191

192

193

194 195

196

197

198

199

200

201202

203

204

205

206

207

208

209

210

211

212213

214

215

216

217

218

219

220

221

222223

224

Where N_{Ex} is the percentage of excess events occurring within a given stress interval, Act is the observed number of events within the interval, and Exp is the expected number of events within the interval assuming a uniform distribution. The problem is reduced to one stress variable to allow the simultaneous evaluation of all earthquakes without assigning ad hoc spatial boundaries to define a region or specific periods of interest. The distribution of Act is populated using the earthquakes in a grid patch with a resolvable background stress tensor to estimate the seasonal stress change projected into the stress components of interest at the time of each event. Similarly, the distribution of Exp is obtained using the same seasonal stress-tensor time-series that is projected into the desired stress component and the values are selected from a uniform distribution of 2500 random times. This approach incorporates all possible stress values at the location of each event. After all stress values are aggregated, the distribution is normalized to equal the equivalent number of actual earthquakes. The stress values are binned in 1.0 kPa stress intervals centered at 0.0 kPa. The stress changes are limited to the range spanning 99% of the population of values. Any events occurring during stress changes beyond these values are included in the end member intervals. This methodology incorporates the complex spatial patterns of the background stress field and the spatiotemporal variations in seasonal loading to assess the relative stress change at the time and location of each earthquake.

3 Results

3.1 Declustered seismicity

For the seismicity declustering model we use the catalog with a M_{min} = 2.0 and events from January 2000 to December 2016. The GRACE acquisitions begin in early 2002, however we include the seismicity beginning in 2000 to improve the seismicity model fitting in the ~3 years before the aftershock sequence of the 2002 M7.9 Denali earthquake located in the study area. The starting catalog contains 20,017 earthquakes and 8,045 independent events after declustering, which effectively removed the aftershock sequence following the 2002 M7.9

Denali earthquake (Figure 3). To evaluate seismicity patterns prior to the GRACE acquisitions we also decluster events going back to 1990, a time period during which the M_c is nearly constant (Figure S1 and S3).

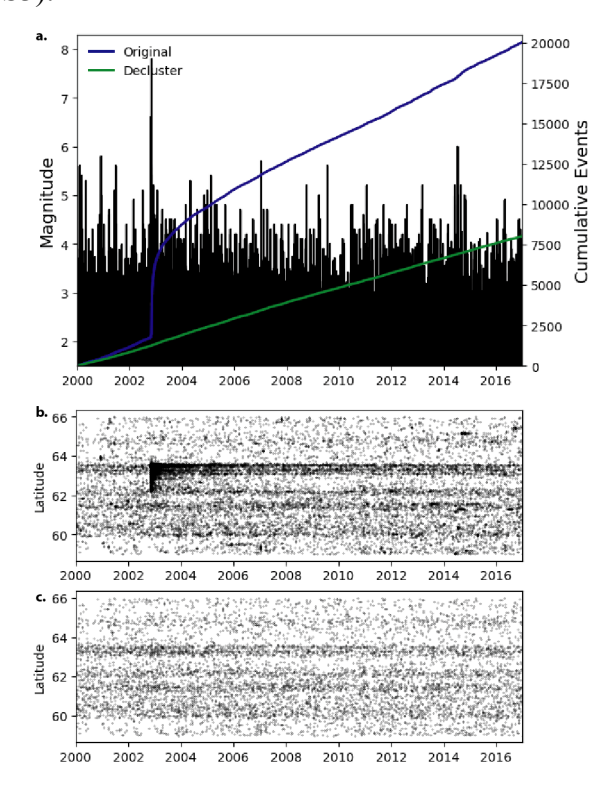


Figure 3. (a) The cumulative shallow seismicity for the original (blue curve) and declustered (green curve) 2000-2016 catalog shown with the magnitudes. (b) The original (top) and declustered (bottom) seismicity shown as time vs latitude to demonstrate the declustering effectively removes the aftershock sequence following the 2002 M7.9 Denali earthquake.

The cumulative number of declustered events indicates a near linear trend of 1.29 events per day, but further inspection reveals additional structure in the data. The declustered seismicity rate is calculated using a 0.25 yr moving window with a 0.083 yr time step (Figure 4a). The time series indicates a prominent seasonal signal in the regional seismicity rate. The spectrum of the seismicity rate indicates a peak at a 1-year period (Figure 4b) and the annual rate variations are also resolvable in the catalog since 1990 (Figure S4). The monthly rate for each year is stacked and shows a change point in seismicity rate throughout the study area starting in the middle of June around day-of-year (DOY) 168 (Figure 5). The rate increases through the end of the year before gradually returning to the lowest rates during the early summer months. To ensure the seasonality is not an artifact of the chosen declustering algorithm, we decluster the same catalog using the nearest-neighbor method [*Zaliapin and Ben-Zion*, 2013] and obtain very similar results with a 1-year signal in the seismicity rate time series (Figures S5 and S6). Additionally, we reduce the magnitude cutoff to M_c1.6 and raise it to M_c2.5 and get very similar results, indicating this is a true feature of the declustered seismicity regardless of parameter or algorithm selection.

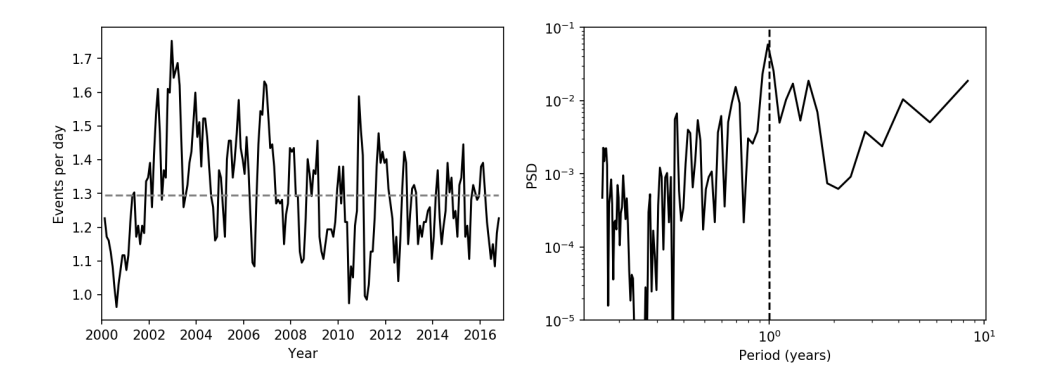


Figure 4. (a) Seismicity rate calculated from the 2000-2016 declustered catalog using a 0.25 yr. moving window and 0.083 yr. step. The gray dashed line is the long-term rate of 1.29 events per day. (b) The periodogram of the seismicity rate showing the power spectral density (PSD) with a vertical dashed line marking 1-year period.

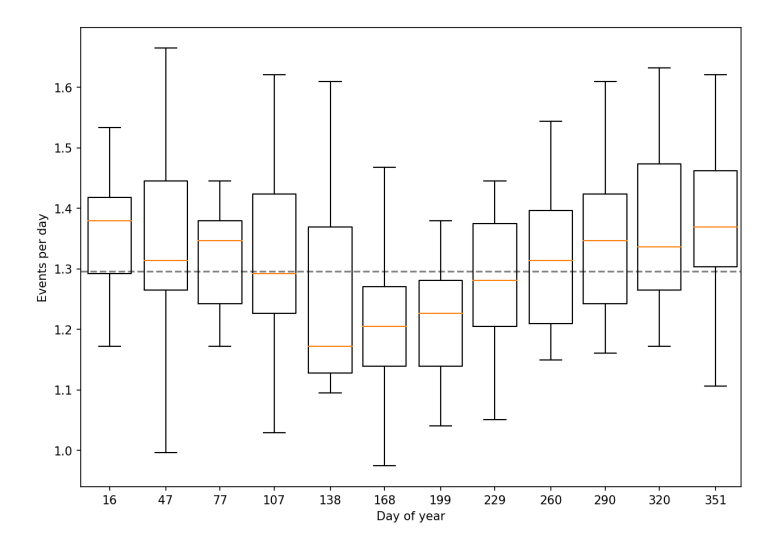


Figure 5. Annual stacked median seismicity rate (orange lines) shown as a box plot indicating the quartile range with vertical lines extending to the full range of yearly values from the 2000-2016 declustered catalog (Figure 3a). The gray dashed line is the long-term rate of 1.29 events per day.

To get a better understanding of the spatiotemporal structure of the seasonal signal, we separate the declustered seismicity on a 0.5° grid and stack all the events in each patch in 12 evenly spaced monthly bins. With a focus on the most seismically active regions, we select all patches that contain more than 40 events in the 16-year-long period (Figure 6a) and for each fit an annual sinusoid model to the monthly stacked seismicity. Average seasonal changes, shown as the ratio of annual modulation amplitude and the annual mean, of 5-50% are observed for much of the region (Figure 6b) with a varying phase (DOY) for the peak in seismicity (Figure 6c). The quality of the seasonal fitting is evaluated with the root mean squared error and is shown to be \leq 2 for much of the region (Figure 6d). Two areas have unusually large numbers of densely spaced earthquakes and exhibit the greatest seasonal change \geq 25% above the average during the peak month. The first is the Kantishna cluster, the most seismically active region in the Alaska interior along the western Denali fault around longitude -151° and latitude 63° [*Ratchkovski and Hansen*, 2002; *Ruppert et al.*, 2008]. The seasonal model fitting shows two

grid locations to the north with up to 40% annual modulation. The peak in seismicity is found to be between DOY 345 – 050 at the grid patches north of the fault and peaking in the summer months and to the south an anticorrelation in the peak time of year is observed. The error in this location is relatively high in comparison to the entire study area. Combining the four grid locations and fitting the seasonal model shows a clearer annual signal with a seasonal variation of eight events with a peak seismicity around DOY 355 (Figure S7). The second region is north of Prince William Sound at longitude -146.5° and latitude 61.5° and shows a peak in seismicity between DOY 200-270. The area to the northwest of Prince William Sound along the Castle Mountain Fault also contains a large number of events with a peak in seismicity between DOY 60-140. We extend this qualitative assessment by evaluating to what degree the stress changes from the seasonal loads enhanced or diminished stress on faults throughout the region by evaluating the loading cycle with respect to the tectonic stress field.

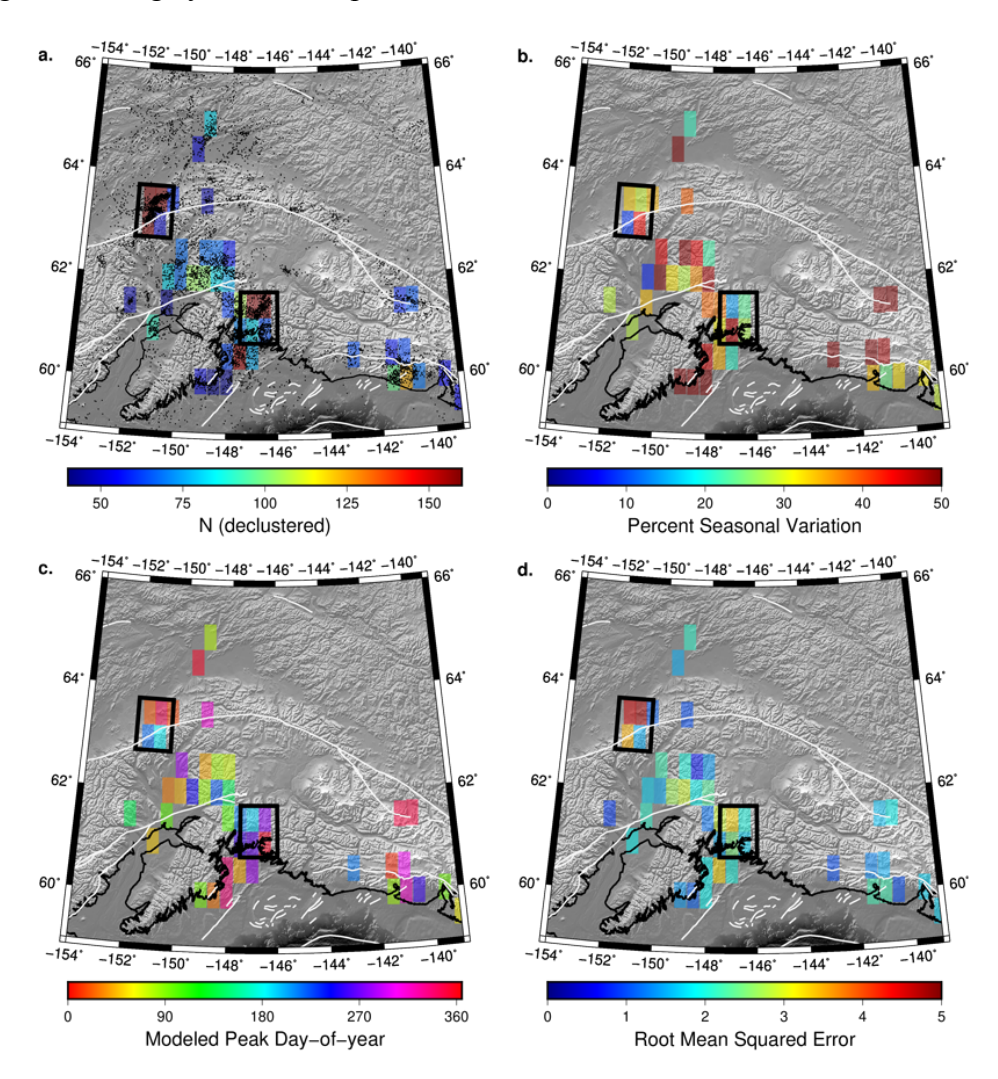


Figure 6. Seasonal models of seismicity. (a) The number of events in each 0.5° grid patch shown with the seismicity (black dots). (b) The percent seasonal change as the ratio of the modeled number of modulated events and the annual mean. (c) The day-of-year of the peak number of events obtained by fitting the stacked monthly event numbers with a seasonal model. (d) The root mean squared error for the model fit. The two black boxes are the locations of the (upper left) west Denali fault and (lower center) Prince William Sound where the largest numbers of events are observed.

3.2 Background stress orientation

268

269

270

271

272

273

274

275

276277

278279

280

281

282283

284

285

286

287

288

289290

The inverted background stress field is presented in Figure 7 as the orientation of the maximum horizontal stress (S_{Hmax}) and the color indicates the faulting style from the shape of the three-dimensional stress tensor [Simpson, 1997]. Shown are the inversion results using an N=10, 6, and 3 minimum number of events in each grid patch. A spatial damping parameter of 2.0 is selected from the elbow of the inversion results tradeoff curve to minimize the data variance and model length (Figure S8). The N=10 tensors are sparse in comparison due to the more rigorous constraints to invert for stress in a grid patch. Decreasing the number of required events to N=6 and N=3 shows similar tensor orientations with higher spatial density that agree well with results obtained by Ruppert [2008]. The tensor dot product for each tensor in the N=10 results with the N=3 results shows no significant change, i.e. a value near 1.0, with the exception of one isolated region to the west (Figure 7d) suggesting the results for the poorly constrained inversion are consistent. A prominent feature extending across the center of the study region is the transpressional strike-slip Denali fault with oblique thrusting consistent with restraining bends and high topography along the fault [Haeussler, 2008; Bemis et al., 2015]. South of the west Denali fault we find oblique thrust faulting in the Peter Hills basin and Susitna basin adjacent to the Talkeetna Mountains north of Anchorage [Haeussler, 2008; Haeussler et al., 2017]. North of Prince William Sound the S_{Hmax} orientation is rotated to about 10° east of north and shows strikeslip faulting consistent with upper plate convergence with S_{Hmax} rotated ~30° to the strike (~235°) of the subducting Yakutat microplate [Chapman et al., 2008]. In the southeast region of the study area, thrust faulting along the coastal ranges transitions to strike slip moving inland, with S_{Hmax} oriented about 330°.

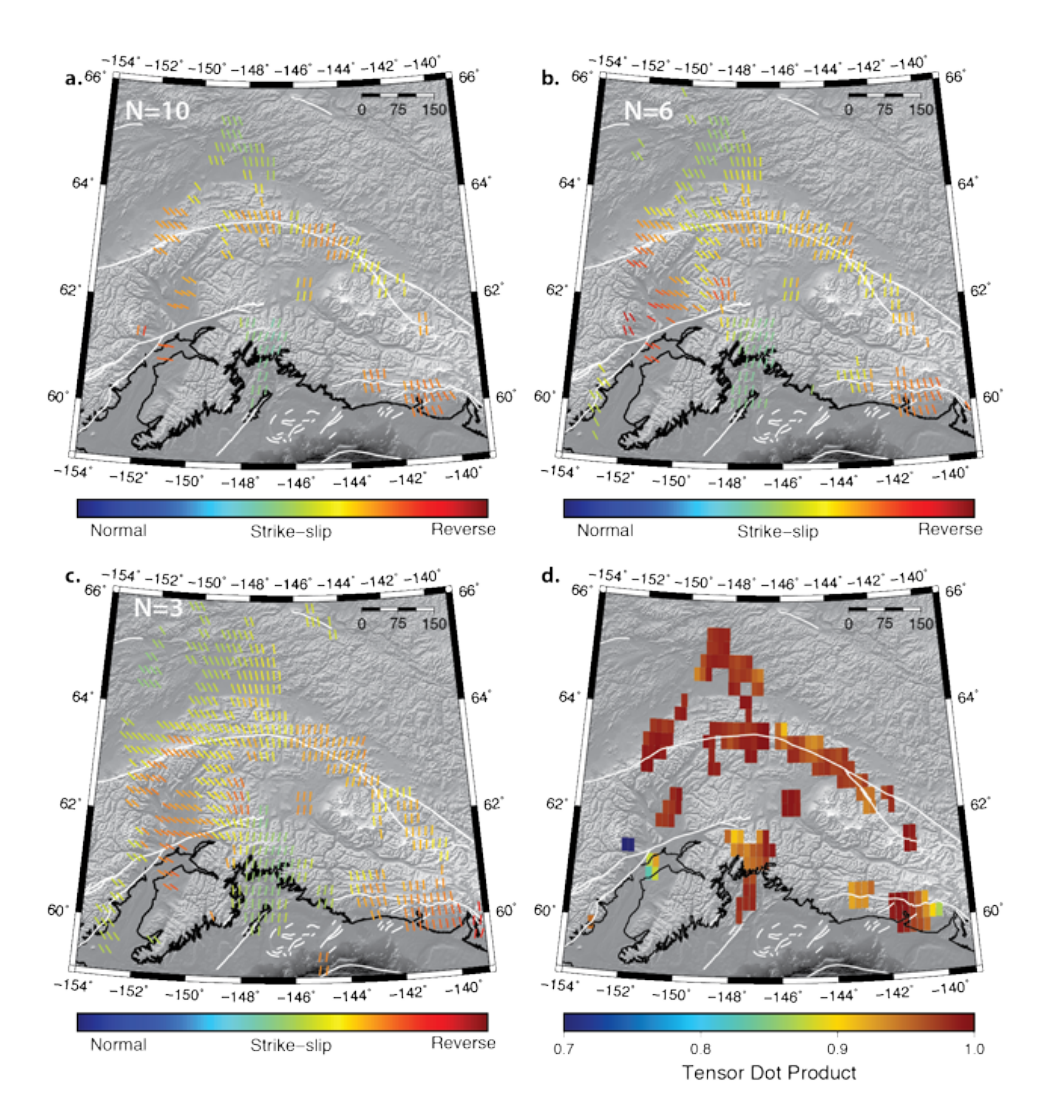


Figure 7. Background stress field (maximum horizontal compressional stress direction) for (a) minimum number of events per grid patch N=10, (b) N=6 events and (c) N=3 events. The color indicates the faulting style from the shape of the three-dimensional stress tensor. (d) The tensor dot product for the N=3 and N=10 three-dimensional stress tensors demonstrating stability of inverted tensor parameters.

3.3 Seasonal stress and seismic response

The seasonal stress change projected into the three-dimensional σ_1 and σ_3 orientations shows a range of peak-to-peak amplitudes between 2-12 kPa across the region (Figure 8a and 8b). The maximum σ_1 amplitude is observed north of Prince William Sound. The Denali fault experiences 4-8 kPa peak-to-peak stress changes in the σ_1 orientation and stresses up to 12 kPa in the σ_3 orientation. Near Prince William Sound the σ_1 and σ_3 stress changes are about 8 and 6 kPa, respectively. In the northern extent of the study area the seasonal stress changes gradually decrease with distance from the loading source (Figure 2). Throughout the region the least compressive seasonal stress in the σ_1 and σ_3 orientation occurs in the fall on DOY ~285 (Figure S9). The differential stress (Figure 8c) varies up to 5 kPa in select locations along all major fault strands. The peak differential stress occurs in the spring months (DOY ~120) along the Denali fault, west Castle Mountain fault, and along the southeast coast. Near Prince William Sound and

to the north the peak occurs around DOY \sim 300 (Figure S9c). The 6-month difference correlates with transpressional regions with a sub-vertical σ_3 orientation in the background stress (Figure 7). The anticorrelation occurs when the seasonal change in the σ_3 orientation exceeds that of the σ_1 orientation during the fall months when the surface load is at a minimum. The change in mean-normal-stress correlates with the location of the load (Figure 2) and is 8 kPa north of Prince William Sound (Figure 8d) and the peak in dilatational stress occurs in the fall months (Figure S9d).

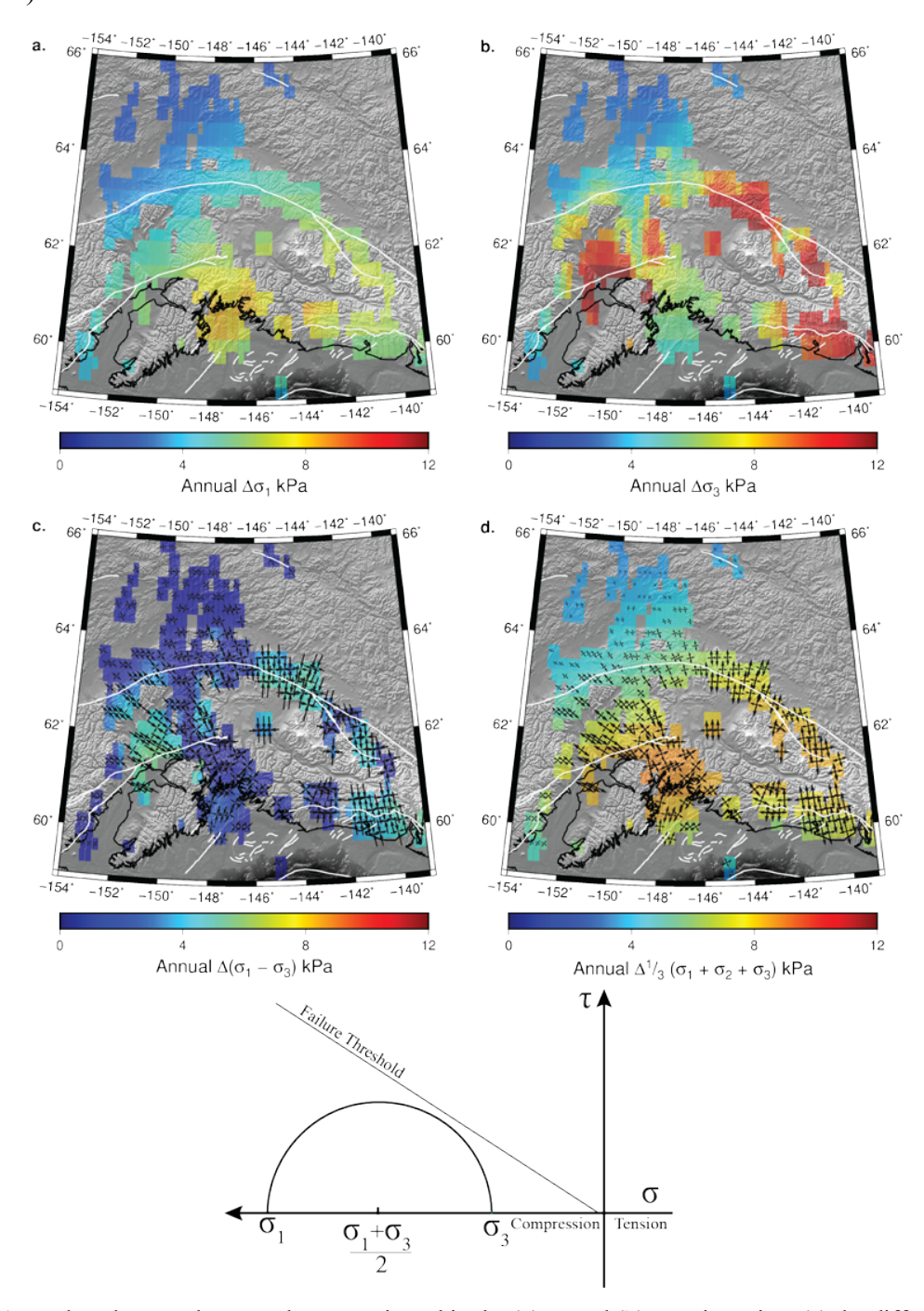


Figure 8. Annual peak-to-peak stress change projected in the (a) σ_1 and (b) σ_3 orientation, (c) the differential stress (σ_1 - σ_3), and (d) the mean-normal-stress (σ_1 + σ_2 + σ_3)/3. The stress orientation sign convention is shown

in the simplified Mohr circle where negative is compression and positive is tension. The peak DOY of the stress change is shown in Figure S9. In panels (c) and (d) the seasonal stress arrows are shown for April 2005 and October 2005, respectively, where outward is extension and inward is compression.

310

311

312

313314

315

316

317

318319

320321

322

323

324

325

326

327328

329330

331

332

333

334

The modulation of seismicity is quantified as the excess percentage of events for four stress-change conditions ($\Delta \sigma_1$, $\Delta \sigma_3$, $\Delta (\sigma_1 - \sigma_3)$, $\Delta (\sigma_1 + \sigma_2 + \sigma_3)/3$) using 5,099 M \geq 2 declustered events that lie within grid patches with stress tensor information. The difference in the total number of events from the declustered catalog (8,045) arises because some earthquakes occur at locations without the background stress tensor information. We evaluate the changes in the seismicity rate with respect to the seasonal stress change at the time of each earthquake. No statistically significant change indicating an increase in seismic activity during seasonal loading is found for any of the stress components tested at the time of each earthquake (Figure S10). The $\Delta \sigma_1$ result would be expected to show excess seismicity for increased compressional stress, but the opposite trend is observed (Figure S10a). The $\Delta \sigma_3$, $\Delta(\sigma_1 - \sigma_3)$, $\Delta(\sigma_1 + \sigma_2 + \sigma_3)/3$ results do suggest the correct trend in the change in seismic activity but the values do not deviate significantly at 95% confidence level from a random background process (Figure 9). To further investigate the observed seasonality in the seismic activity and surface loads, we test time lags from 1 to 5 months. A weak correlation at 2 months is observed, however the 3-month time lag shows the strongest correlation with a 25% deviation from background seismicity rates during the 8 kPa annual modulation of mean-normal-stress (Figure 9d). Excess events of 3.5% per kPa are found as the pressure at seismogenic depths decreases. Considering stress changes in the σ_1 and σ_3 orientations, the correlation with σ_3 indicates the expected change in seismicity for reduced compression. The $\Delta(\sigma_1 - \sigma_3)$ results show a positive correlation indicating the seasonal variation in the $\Delta \sigma_3$ orientation is larger than the $\Delta \sigma_1$ orientation, which will increase the diameter of the Mohr circle and move the system closer to the failure plane. The results suggest a decrease in mean-normal-stress and increase in differential stress are modulating seismic activity through a mechanism that is producing an approximately 3-month delayed seismic response of the regional fault systems. The results provide insight to a possible delayed earthquake triggering mechanism.

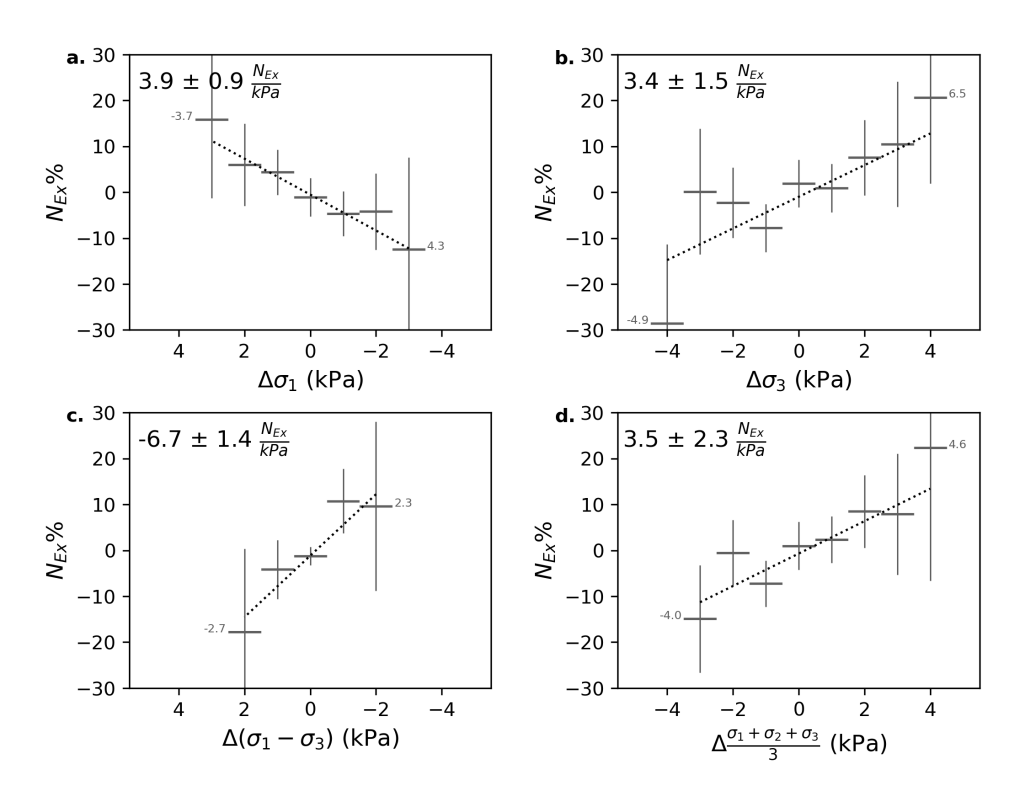


Figure 9. The percent excess seismicity considering a 3-month time lag for a seismic response due to stress changes in the (a) σ_1 orientation, (b) σ_3 orientation, (c) differential stress (σ_1 - σ_3), and (d) the mean-normal-stress. Negative stress values indicate compression and positive values are tension. Note the x-axis for (a) and (c) are reversed so that a positive slope indicates a positive correlation in all four panels. The stress intervals of 1 kPa are shown by the horizonal bars and the vertical bars indicate the 95% confidence intervals. The trend of the best-fit line is shown in the top left of each panel with the 2-sigma error and shown as the dotted line.

The region-wide results suggest a subsurface change in pressure is modulating seismic activity but is not found to be statistically significant for an instantaneous response across the entire study area (Figure S10). Site specific time series of the west Denali fault and Prince William Sound regions show the variability of the seasonal mean-normal-stress amplitude with the local seismicity (Figure 10). The two regions show similar features in the seismicity time series and both indicate a time lag between the peak stress and seismicity rate, with the peak stress in the fall months. The maximum cross correlation coefficient is ~0.2 at a lag time of 2 and 6 months for the west Denali fault and Prince William Sound regions, respectively. Inspection of the time series suggests a low correlation due to the non-stationarity of the trend of the seismicity rate and variations in activity at periods other than the annual cycle. The annual stacked seismicity shows the lowest number of events along the Denali fault during June. For the Prince William Sound region, the seasonal signal is less pronounced but a systematic reduction in seismic activity is observed in June. Stacking the annual time series highlights the seasonal loading modulating the background stress components. For the west Denali fault the reduced compression in the σ_3 orientation is greater than in the σ_1 orientation, thereby producing increased differential stress in the spring. This is not observed in the Prince William Sound region that is closer to the peak source of loading and in a transtensional setting, where the modulation in the σ_1 orientation is expected to vary the greatest from a vertical surface load.

335

336

337

338339

340

341

342343

344

345

346

347

348

349

350

351

352

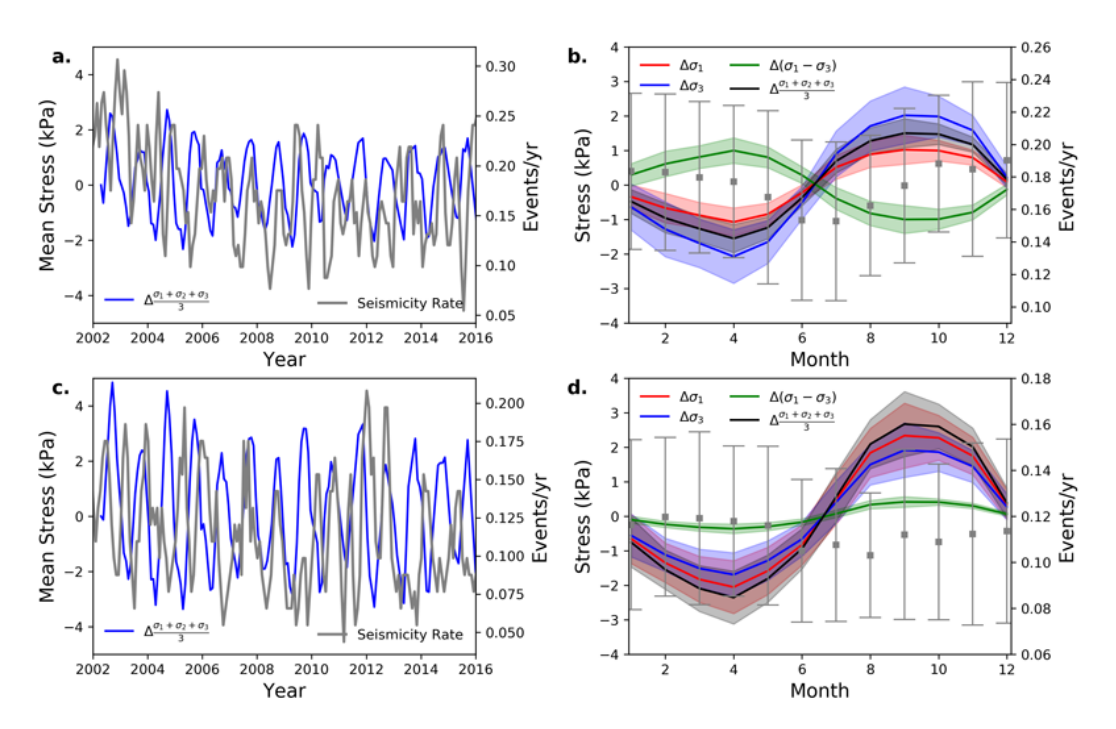


Figure 10. Seasonal stress change time series from 2002 to 2016 for the mean-normal-stress (blue curve) shown with the seismicity rate (gray curve) for (**a**) west Denali fault (-151.0°, 63.0°) and (**c**) Prince William Sound (-146.5°, 61.0°) as indicated in Figure 6. Note the seismicity rate variation for the west Denali fault is 2 times the observation at Prince William Sound. The monthly average stress change with 1 standard deviation (**b** and **d**) for the four stress components are shown to highlight the variability in seasonal loading for different tectonic environments. The monthly average seismicity rate with 1 standard deviation is shown in gray (**b** and **d**). In panel (**b**) the differential stress shows the 6-month phase shift as indicated in Figure S9.

4 Discussion

354

355

356

357

358

359

360

361

362

363

364

365

366

367

368

369

370

371

372

373

Southern Alaska experiences seasonal hydrological loads of up to 0.5 m of equivalent water storage (Figure 2) that cause vertical ground displacements of a few centimeters [Fu et al., 2012]. The mass change from snow, rain, and glaciers results in crustal stress perturbations in the upper 10 km of about 10 kPa in the σ_1 and σ_3 orientations of the ambient stress field (Figure 8). The cyclic loading produces a reduction in mean-normal-stress during the late summer and fall when the surface mass is near the annual minimum. A decrease in mean-normal-stress is effectively a decrease in pressure. The peak in this stress cycle corresponds to the lowest regionwide seismicity rates during the summer and early fall for crustal faults above the subduction zone (Figure 5). If the amplitude of cyclic loading is the same order of magnitude as the tectonic loading rate multiplied by the period of interest, then the modulation of seismicity is expected to correlate with the peak stress; if the cyclic loading is less, then the correlation is expected to occur with the peak stressing rate [Ader et al., 2014]. The interseismic crustal shear stressing rates vary from 1-10 kPa/yr with lower values north along the Denali Fault and increase up to 10 kPa/yr along the coast, about 150 km inland from the offshore plate boundary; the compressional stressing rates show the same spatial variation and range from -1 - -40 kPa/yr [Ali and Freed, 2010]. The interior regions with lower crustal stressing rates would increase the critical period for a cyclic loading response to longer, interannual time scales [Ader et al., 2014; Craig et al., 2017], while the coastal regions would be expected to be more responsive to the annual cycle. The results presented in Figure 9 show seismic activity exceeding background levels with a 3month time lag during the ~8 kPa annual change in mean-normal-stress, differential stress, and least principal compressive stress. A correlation with the peak stressing rate is not observed (Figure S11) and any correlation with the stressing rate in Alaska would require more earthquakes to occur prior to the peak amplitude, not during the months following. The time lag of 2-6 months from a pressure decrease suggests fluid diffusion, or another time dependent process, is influencing the rate changes. Evaluating the entire region collectively could potentially be affected by contributions from multiple processes and different loading environments, which may influence the observed delay times.

374

375

376377

378379

380 381

382

383

384

385

386

387

388

389

390

391

392393

394

395

396

397

398

399400

401

402

403

404

405 406

407 408

409

410

411

412

413

414

415

416

417

418

One might expect the time of year for peak loading conditions to vary due to the spatial heterogeneity of the regional fault geometries [e.g. *Craig et al.*, 2017; *Johnson et al.*, 2017b]. However, the long-wavelength loading signal in southern Alaska is best resolved as a change in subsurface pressure that peaks at the same time of the year without significant correlation in the principal stress component orientations (Figures 2 and 8). In Alaska the southern coastal regions experience seasonal precipitation that peaks in the fall, then snow accumulation throughout the winter months, creating a scenario where surface loading can vary on length scales not resolvable at the 300 km resolution of GRACE. A higher spatiotemporal resolution of the annual hydrospheric loading than observed by GRACE is required [e.g. *Johnson et al.*, 2017a] for further separating of seasonally modulated earthquakes occurring either instantaneously or delayed with respect to the timing of the loading cycle.

Hydrological forcing can alter the timing of earthquake occurrence through direct surface loading that modulates crustal stresses or pore pressure variations at seismogenic depths with a time delay. The lack of an immediate correlated seismic response for the shallow crustal fault systems in southern Alaska suggests a time dependent process is modulating the annual seismicity rates. The two regions highlighted in Figure 10 show time lags of 2-6 months from the peak reduction of mean-normal-stress with the interannual changes in seismicity rates, which are possibly the result of other tectonic or climatic processes influencing the timing of seismic events. If the modulation is driven by exceeding a failure threshold we would expect an instantaneous response [Beeler and Lockner, 2003] but instead we find a time lag between the peak stress amplitude and seismicity, which peaks during the winter and spring months. This observation contrasts with the timing of large-magnitude events on the subduction slab interface in Japan that occur less often during the winter months as snow loading increases the compressional normal stresses and slows the rate of strain accumulation, thereby inhibiting earthquake nucleation until the summer months [Heki, 2003]. The variations in shallow crustal events in Japan are similar to our observations of increased activity in the fall months, but we are not finding a second increase in seismicity during the spring that is possibly related to pore pressure changes from precipitation [*Ueda and Kato*, 2019]. Another contrasting scenario is observed in the Himalaya following the summer monsoons in the Ganges Basin; the decrease in surface loading during the winter months increases the stressing rate on the Main Himalaya Thrust fault to produce more events in the winter [Bettinelli et al., 2008]. In Alaska, the 3-month time lag suggests a change in crustal pore pressure is a possible source modulating seismicity [Wolf et al., 1997]. However, it is likely that the heterogeneous faulting network throughout southern Alaska would produce differing diffusion time lags, some instantaneous triggering, or delayed triggering in response to the seasonal loading cycle.

Deconvolving the underlying physical mechanism of triggered earthquakes from a known source of transient stress can become ambiguous when considering a delay time in the perturbed

system. *Craig et al.* [2017] find an inverse correlation with peak loading and seismicity on a multi-year hydrological loading signal making a pore-fluid pressure-effect unlikely. If we assume a depth of 10 km, the time delay from a simple 1D diffusion process [e.g. *Shapiro*, 2015] would be 0.25 and 2.5 years for a diffusivity of 1.0 and 0.1 m²/s, respectively, making the possibility of an overall 3 month time lag in Alaska highly unlikely. A plausible scenario is increased mobility throughout the annual loading cycle of preexisting water at seismogenic depths, where changes in fluid pressure on the faults could result in the delay time observed in the seismic data [e.g. *Cocco and Rice*, 2002]. Fluid originating at the surface can explain shallow seismicity variations [e.g. *Hainzl et al.*, 2013] but requires an unreasonably high diffusivity value (e.g. D>1.0) to invoke an induced pressure wave at 10 km depth when considering the increased confining pressure. The results show additional modeling of subsurface fluid mobility could provide insight to the triggering mechanism responsible for the observed seismic activity and any effort to constrain crustal hydrological properties should focus on annual and interannual time scale to reduce ambiguity in the physical forcing mechanism [*Craig et al.*, 2017].

More work is required to explore the triggering relationships over a wider range of time scales and modulation of seismicity on the plate interface of the subducting slab. The long-term load reduction from melting glaciers is shown to produce increases in the seismic strain release as a function of glacial retreat during warmer and cooler years [Sauber and Molnia, 2004]. On the annual scale this process constructively interferes with the long-term mass wastage that is greatest in the summer months and correlates with localized changes in seismic activity [Sauber and Ruppert, 2008]. The shallow crustal faults explored in this study exhibit seismicity rate changes of lower-magnitude earthquakes that provide evidence for the timing of earthquake nucleation due to transient stress changes. Further investigation is needed to assess the stress changes on the plate interface and within the subducting oceanic lithosphere at much greater depths, which have previously hosted large magnitude events, and evaluate the possibility of modulation of seismic activity beyond the shallow crustal fault systems and on longer time scales.

5 Conclusions

Evidence is presented for the annual modulation of seismic activity on shallow crustal faults in southern Alaska from hydrological loading. The seismicity catalog is declustered to remove aftershocks and an annual rate variation in the seismicity is observed, with the greatest number of earthquakes occurring during the winter months. The GRACE constrained stress timeseries is projected into the background stress tensor and reveals no correlation with increased compressive stress in the $\Delta\sigma_1$ orientation. Instead a correlation is observed with a 3-month time lag from the peak reduction in mean-normal-stress, the differential stress, and least principal compressive stress, suggesting a delayed process is modulating seismicity after subsurface pressure is reduced. Fluid diffusion from surface waters is a plausible forcing mechanism but is an unlikely explanation for our results, since a homogenous pore-fluid pore-pressure change would be required across the large region with heterogenous fault structures. More plausible is the increased fluid mobility of preexisting subsurface waters that modulates pressure on the fault on varying time scales throughout the annual loading cycle. The variations in lower magnitude seismicity rates provides additional evidence for the modulation of earthquake activity from stress changes of <10kPa observed during annual surface loading cycles.

Acknowledgments

462

- The authors thank Editor Jean-Philippe Avouac and two reviewers for constructive comments
- that help improve the manuscript. C.W. Johnson is funded by the National Science Foundation
- EAR Postdoctoral Fellowship award 1725344. The project is supported by NASA Earth Surface
- and Interior grant NNX17AE01G. The study utilizes publicly available seismicity data through
- the Alaska Earthquake Center (earthquake.alaska.edu) and we thank Natalia Ruppert and Carl
- Tape for assistance obtaining the complete seismicity catalogs. The GRACE solutions are
- publicly available through the Jet Propulsion Laboratory (ftp://podaac-
- ftp.jpl.nasa.gov/allData/tellus/L3/mascon/RL05/JPL/CRI/netcdf/). Figures were produced using
- 471 GMT and Matplotlib.

472 **References**

- Ader, T. J., N. Lapusta, J.-P. Avouac, and J.-P. Ampuero (2014), Response of rate-and-state
- seismogenic faults to harmonic shear-stress perturbations, *Geophysical Journal*
- 475 International, 198(1), 385-413, doi:10.1093/gji/ggu144.
- Ali, S. T., and A. M. Freed (2010), Contemporary deformation and stressing rates in Southern
- 477 Alaska, Geophysical Journal International, 183(2), 557-571, doi:10.1111/j.1365-
- 478 246X.2010.04784.x.
- Amos, C. B., P. Audet, W. C. Hammond, R. Burgmann, I. A. Johanson, and G. Blewitt (2014),
- 480 Uplift and seismicity driven by groundwater depletion in central California, *Nature*,
- 481 509(7501), 483-486, doi:10.1038/nature13275.
- Beeler, N. M., and D. A. Lockner (2003), Why earthquakes correlate weakly with the solid Earth
- 483 tides: Effects of periodic stress on the rate and probability of earthquake occurrence,
- 484 *Journal of Geophysical Research*, 108(B8), doi:10.1029/2001jb001518.
- Bemis, S. P., R. J. Weldon, and G. A. Carver (2015), Slip partitioning along a continuously
- 486 curved fault: Quaternary geologic controls on Denali fault system slip partitioning,
- growth of the Alaska Range, and the tectonics of south-central Alaska, *Lithosphere*, 7(3),
- 488 235-246, doi:10.1130/l352.1.
- Bettinelli, P., J.-P. Avouac, M. Flouzat, L. Bollinger, G. Ramillien, S. Rajaure, and S. Sapkota
- 490 (2008), Seasonal variations of seismicity and geodetic strain in the Himalaya induced by
- 491 surface hydrology, Earth and Planetary Science Letters, 266(3-4), 332-344,
- doi:10.1016/j.epsl.2007.11.021.
- 493 Bollinger, L., F. Perrier, J. P. Avouac, S. Sapkota, U. Gautam, and D. R. Tiwari (2007), Seasonal
- modulation of seismicity in the Himalaya of Nepal, Geophysical Research Letters, 34(8),
- doi:10.1029/2006GL029192.
- Chapman, J. B., et al. (2008), Neotectonics of the Yakutat Collision: Changes in Deformation
- Driven by Mass Redistribution, in *Active Tectonics and Seismic Potential of Alaska*,
- 498 edited, pp. 65-81, doi:10.1029/179gm04.

499	Christiansen, L. B., S. Hurwitz, and S. E. Ingebritsen (2007), Annual modulation of seismicity
500	along the San Andreas Fault near Parkfield, CA, Geophysical Research Letters, 34(4),
501	doi:10.1029/2006g1028634

- Cocco, M., and J. R. Rice (2002), Pore pressure and poroelasticity effects in Coulomb stress analysis of earthquake interactions, *Journal of Geophysical Research: Solid Earth*, 107(B2), ESE 2-1-ESE 2-17, doi:10.1029/2000jb000138.
- Craig, T. J., K. Chanard, and E. Calais (2017), Hydrologically-driven crustal stresses and seismicity in the New Madrid Seismic Zone, *Nature Communications*, 8(1), 2143, doi:10.1038/s41467-017-01696-w.
- Dziewonski, A. M., and D. L. Anderson (1981), Preliminary reference Earth model, *Physics of the Earth and Planetary Interiors*, *25*(4), 297-356, doi:http://dx.doi.org/10.1016/0031-9201(81)90046-7.
- Eberhart-Phillips, D., et al. (2003), The 2002 Denali Fault Earthquake, Alaska: A Large Magnitude, Slip-Partitioned Event, *Science*, *300*(5622), 1113-1118, doi:10.1126/science.1082703.
- Felzer, K. R., T. W. Becker, R. E. Abercrombie, G. Ekström, and J. R. Rice (2002), Triggering of the 1999 MW 7.1 Hector Mine earthquake by aftershocks of the 1992 MW 7.3 Landers earthquake, *Journal of Geophysical Research: Solid Earth*, *107*(B9), ESE 6-1-517 ESE 6-13, doi:10.1029/2001JB000911.
- Freed, A. M. (2005), Earthquake Triggering by Static, Dynamic, and Postseismic Stress
 Transfer, *Annual Review of Earth and Planetary Sciences*, *33*(1), 335-367,
 doi:10.1146/annurev.earth.33.092203.122505.
- Fu, Y., J. T. Freymueller, and T. Jensen (2012), Seasonal hydrological loading in southern Alaska observed by GPS and GRACE, *Geophysical Research Letters*, *39*(15), doi:10.1029/2012GL052453.
- Gardner, J. K., and L. Knopoff (1974), Is the sequence of earthquakes in Southern California, with aftershocks removed, Poissonian?, *Bulletin of the Seismological Society of America*, 64(5), 1363-1367.
- Haeussler, P. J. (2008), An Overview of the Neotectonics of Interior Alaska: Far-Field
 Deformation from the Yakutat Microplate Collision, in *Active Tectonics and Seismic Potential of Alaska*, edited, pp. 83-108, doi:10.1029/179GM05.
- Haeussler, P. J., R. W. Saltus, R. G. Stanley, N. Ruppert, K. Lewis, S. M. Karl, and A. Bender (2017), The Peters Hills basin, a Neogene wedge-top basin on the Broad Pass thrust fault, south-central Alaska, *Geosphere*, *13*(5), 1464-1488, doi:10.1130/ges01487.1.
- Hainzl, S., Y. Ben-Zion, C. Cattania, and J. Wassermann (2013), Testing atmospheric and tidal earthquake triggering at Mt. Hochstaufen, Germany, *Journal of Geophysical Research:* Solid Earth, 118(10), 5442-5452, doi:10.1002/jgrb.50387.

- Hainzl, S., T. Kraft, J. Wassermann, H. Igel, and E. Schmedes (2006), Evidence for rainfall-
- triggered earthquake activity, Geophysical Research Letters, 33(19),
- doi:10.1029/2006GL027642.
- Hardebeck, J. L., and A. J. Michael (2006), Damped regional-scale stress inversions:
- Methodology and examples for southern California and the Coalinga aftershock
- sequence, Journal of Geophysical Research, 111(B11), doi:10.1029/2005jb004144.
- Hardebeck, J. L., and P. M. Shearer (2002), A New Method for Determining First-Motion Focal
- Mechanisms, Bulletin of the Seismological Society of America, 92(6), 2264-2276,
- 544 doi:10.1785/0120010200.
- Heki, K. (2003), Snow load and seasonal variation of earthquake occurrence in Japan, *Earth and Planetary Science Letters*, 207(1), 159-164, doi:10.1016/S0012-821X(02)01148-2.
- Johnson, C. W., Y. Fu, and R. Bürgmann (2017a), Seasonal water storage, stress modulation, and California seismicity, *Science*, *356*(6343), 1161-1164, doi:10.1126/science.aak9547.
- Johnson, C. W., Y. Fu, and R. Bürgmann (2017b), Stress Models of the Annual Hydrospheric,
- Atmospheric, Thermal, and Tidal Loading Cycles on California Faults: Perturbation of
- Background Stress and Changes in Seismicity, Journal of Geophysical Research: Solid
- *Earth*, 122(12), 10,605-610,625, doi:10.1002/2017JB014778.
- Larsen, C. F., E. Burgess, A. A. Arendt, S. O'Neel, A. J. Johnson, and C. Kienholz (2015),
- Surface melt dominates Alaska glacier mass balance, *Geophysical Research Letters*,
- 555 42(14), 5902-5908, doi:10.1002/2015GL064349.
- O'Neel, S., C. F. Larsen, N. Rupert, and R. Hansen (2010), Iceberg calving as a primary source
- of regional-scale glacier-generated seismicity in the St. Elias Mountains, Alaska, *Journal*
- of Geophysical Research: Earth Surface, 115(F4), doi:10.1029/2009jf001598.
- O'Neel, S., H. P. Marshall, D. E. McNamara, and W. T. Pfeffer (2007), Seismic detection and
- analysis of icequakes at Columbia Glacier, Alaska, *Journal of Geophysical Research*:
- *Earth Surface*, 112(F3), doi:10.1029/2006jf000595.
- Pollitz, F. F., A. Wech, H. Kao, and R. Bürgmann (2013), Annual modulation of non-volcanic
- tremor in northern Cascadia, Journal of Geophysical Research: Solid Earth, 118(5),
- 564 2445-2459, doi:10.1002/jgrb.50181.
- Ratchkovski, N. A., and R. A. Hansen (2002), New Constraints on Tectonics of Interior Alaska:
- Earthquake Locations, Source Mechanisms, and Stress Regime, *Bulletin of the*
- *Seismological Society of America*, *92*(3), 998-1014, doi:10.1785/0120010182.
- Ruppert, N. A. (2008), Stress Map for Alaska from Earthquake Focal Mechanisms, in *Active*
- Tectonics and Seismic Potential of Alaska, edited, pp. 351-367, American Geophysical
- 570 Union, doi:10.1029/179GM20.

- Ruppert, N. A., and R. A. Hansen (2010), Temporal and Spatial Variations of Local Magnitudes
- in Alaska and Aleutians and Comparison with Body-Wave and Moment Magnitudes,
- *Bulletin of the Seismological Society of America*, 100(3), 1174-1183,
- 574 doi:10.1785/0120090172.
- Ruppert, N. A., K. D. Ridgway, J. T. Freymueller, R. S. Cross, and R. A. Hansen (2008), Active
- Tectonics of Interior Alaska: Seismicity, Gps Geodesy, and Local Geomorphology, in
- Active Tectonics and Seismic Potential of Alaska, edited, pp. 109-133,
- 578 doi:10.1029/179GM06.
- Sauber, J. M., and B. F. Molnia (2004), Glacier ice mass fluctuations and fault instability in
- tectonically active Southern Alaska, *Global and Planetary Change*, 42(1), 279-293,
- doi:https://doi.org/10.1016/j.gloplacha.2003.11.012.
- Sauber, J. M., and N. A. Ruppert (2008), Rapid Ice Mass Loss: Does It Have an Influence on
- Earthquake Occurrence in Southern Alaska?, in *Active Tectonics and Seismic Potential of*
- Alaska, edited, pp. 369-384, American Geophysical Union, doi:10.1029/179GM21.
- Shapiro, S. A. (2015), *Fluid-Induced Seismicity*, Cambridge University Press.
- Simpson, R. W. (1997), Quantifying Anderson's fault types, *Journal of Geophysical Research*:
- 587 Solid Earth, 102(B8), 17909-17919, doi:10.1029/97JB01274.
- Toda, S., R. S. Stein, G. C. Beroza, and D. Marsan (2012), Aftershocks halted by static stress
- shadows, *Nature Geoscience*, 5, 410, doi:10.1038/ngeo1465.
- 590 Ueda, T., and A. Kato (2019), Seasonal Variations in Crustal Seismicity in San-in District,
- Southwest Japan, Geophysical Research Letters, 46(6), 3172-3179,
- 592 doi:10.1029/2018gl081789.
- Watkins, M. M., D. N. Wiese, D.-N. Yuan, C. Boening, and F. W. Landerer (2015), Improved
- methods for observing Earth's time variable mass distribution with GRACE using
- spherical cap mascons, Journal of Geophysical Research: Solid Earth, 120(4), 2648-
- 596 2671, doi:10.1002/2014JB011547.
- Woessner, J., and S. Wiemer (2005), Assessing the Quality of Earthquake Catalogues:
- Estimating the Magnitude of Completeness and Its Uncertainty, *Bulletin of the*
- *Seismological Society of America*, *95*(2), 684-698, doi:10.1785/0120040007.
- Wolf, L. W., C. A. Rowe, and R. B. Horner (1997), Periodic seismicity near Mt. Ogden on the
- Alaska-British Columbia border: A case for hydrologically triggered earthquakes?,
- Bulletin of the Seismological Society of America, 87(6), 1473-1483.
- Zaliapin, I., and Y. Ben-Zion (2013), Earthquake clusters in southern California I: Identification
- and stability, Journal of Geophysical Research: Solid Earth, 118(6), 2847-2864,
- doi:10.1002/jgrb.50179.

Zhuang, J., Y. Ogata, and D. Vere-Jones (2002), Stochastic Declustering of Space-Time
Earthquake Occurrences, Journal of the American Statistical Association, 97(458), 369-
380, doi:10.1198/016214502760046925.